PCCP

ROYAL SOCIETY OF CHEMISTRY

PAPER

View Article Online
View Journal | View Issue

Cite this: *Phys. Chem. Chem. Phys.*, 2026, **28**, 3016

Intra- and intermolecular H-bonds and π–π stacking driven organization of a triazine-based room temperature phosphorescent emitter†

Daniele Malpicci, [ab] Elena Lucenti, [b] Luca Zecchinello, [ab] Daniele Marinotto, [b] Elena Cariati *[ab] and Alessandra Forni *[b]

Received 24th September 2025,
Accepted 18th December 2025

DOI: 10.1039/d5cp03691g

rsc.li/pccp

Excitation dependent, multiemissive single component organic materials are receiving evergrowing attention for various applications. In this regard, intermolecular interactions have been revealed to be efficacious in positively affecting photoluminescence features. Here, the photophysical properties of **TT-2PyH$^+$NO$_3^-$** characterized by fluorescence and dual phosphorescence with ultralong contributions, are interpreted through DFT-TDDFT calculations and crystal structure analysis. The compound's locked molecular conformation through an intramolecular hydrogen bond is at the basis of suppression of the low energy fluorescence displayed by its parent neutral derivative. On the other side, π–π interactions are deemed responsible for the ultralong RTP features and the highly dense network of intermolecular hydrogen bonds provides a rigid molecular environment which efficiently restricts the non-radiative deactivation channels of triplet excitons.

Introduction

Organic single component materials characterized by rich emissive behavior, comprising molecular and possibly supramolecular excitation-dependent fluorescence and room temperature phosphorescence (RTP), are receiving increasing attention from the scientific community due to the advantages they offer in different fields (*e.g.* bioimaging,[1–3] anticounterfeiting,[4–8] and displays[9]). In particular, the number of purely organic long-lived phosphors is rapidly growing thanks to the advancements in molecular design and supramolecular engineering aimed at promoting singlet-to-triplet intersystem crossing (ISC) and suppressing non-radiative decay from excited triplet states.[10–14]

Particularly important, in this context, are organic compounds displaying ultralong RTP, a persistent luminescence with emission lifetimes of over 100 ms. To achieve RTUP, a rigid molecular environment, able to reduce molecular motions and thus stabilize the triplet excitons from nonradiative decay, represents a necessary condition. To this aim, several types of intra- and intermolecular interactions, including hydrogen bonds, halogen bonds, ionic bonds, and π–π interactions, have been exploited.[15–23] Notably, hydrogen bonding has been demonstrated to be particularly efficacious in rigidifying the molecular conformations and decreasing non-radiative deactivation channels of triplet excitons, contributing to phosphorescence lifetimes and enhancing quantum yield.[24–26]

As a contribution to this important research field, we have recently developed a wide family of compounds based on triimidazo[1,2-*a*:1′,2′-*c*:1″,2″-*e*][1,3,5]triazine or cyclic triimidazole (hereafter **TT**), characterized by a rich photophysical behavior comprising multiple fluorescence and phosphorescence of molecular and supramolecular origins, anti-Kasha emissions and excitation-dependent photoluminescence.[27] In the **TT** prototype itself, the role of π–π interactions in activating radiative deactivation channels (fluorescence and RTUP lasting up to 1 s) through distortion of the C_{3h} symmetry has been highlighted. Moreover, for many **TTs**, π–π interactions were demonstrated to be relevant in influencing their photophysics and responsible for their mechanochromic features.

In this context, previous studies on 3-(pyridin-2-yl)triimidazotriazine (**TT-2Py**), the pyridine derivative with the pyridinic nitrogen atom in the ortho position with respect to **TT**, revealed a multifaceted, excitation-dependent emissive behaviour comprising dual fluorescence and multiple phosphorescence.[28,29] The origin of each contribution was explained, through deep experimental and theoretical investigation, on the basis of its molecular and supramolecular features.[28] In particular, the role of the partial rotational freedom of the pyridine ring in the compound's photoluminescence was disclosed. In addition to its

[a] *Department of Chemistry, Università degli Studi di Milano, via Golgi 19, 20133, Milano, Italy. E-mail: elena.cariati@unimi.it*
[b] *Institute of Chemical Sciences and Technologies "Giulio Natta" (SCITEC) of CNR, via Golgi 19, 20133, Milano, Italy. E-mail: alessandra.forni@scitec.cnr.it*

† Dedicated to Professor Resnati, celebrating a career in fluorine and noncovalent chemistry on the occasion of his 70th birthday.

appealing emissive properties, this compound was revealed to be highly efficient in the preparation of coordination complexes and coordination polymers (CPs),[30–32] thanks to the coordinating ability of pyridine and **TT** itself.[33–35] Among metal containing derivatives, particularly noteworthy in view of its photoluminescence properties is the emissive Cu(I)-based CP, displaying an intriguing and rare structural motif comprising a double-stranded $(CuI)_2$ stair and a single CuI zig-zag chain.[30]

Here, after a brief recap of the structural and photophysical features of **TT-2Py**, we report on the synthesis, characterization and photophysical investigation of its protonated derivative, **TT-2PyH$^+$**. Besides revealing interesting photophysical properties, including dual phosphorescence with ultralong contribution, this compound displays a locked molecular conformation through an intramolecular hydrogen bond (HB), which is demonstrated to be responsible for the suppression of the low energy fluorescence of the parent neutral derivative, supporting previous interpretation of the photophysical behaviour.

Results and discussion

According to previous studies, **TT-2Py** was isolated in three polymorphs depending on the recrystallization solvent.[28] All of them display, in their crystal structure, π–π stacking interactions among **TT** moieties, characterized by slightly different intermolecular distances and slippage features. The **TT** units are further anchored to each other by several short C–H···N HBs in a plane roughly perpendicular to the stacking axis. On the other hand, the pyridinic ring, slightly rotated with respect to the **TT** plane, is involved only in weak interactions resulting in conformational freedom, which is at the basis of the formation of the three polymorphs.

Extensive spectroscopic, structural and theoretical investigation on **TT-2Py** evidenced the presence of both molecular and supramolecular radiative deactivation channels in its complex solid-state photophysical behavior (see Table 1 and Fig. 1). In particular, π–π interactions among **TT** units were deemed responsible for low energy phosphorescence (LEP), while the remaining emissions, namely HEF (high energy fluorescence), HEP (high energy phosphorescence), MEP (medium energy

Table 1 Photophysical parameters of the crystals of **TT-2Py** (polymorph **A**), blended **TT-2Py**/PMMA (w/w 10%) films and crystals of **(TT-2PyH$^+$NO$_3^-$)·H$_2$O**

298 K				
	Φ	λ_{em} (nm)	τ	Origin
TT-2Py (polymorph A)	52	370	698 ms	HEP
		418	0.29 ms	MEP
		450		LEF
		510, 570, 608	2.09 ms	LEP
TT-2Py/PMMA		350	1.18 ns	HEF
		394	13.73 ms	MEP
		440	3.47 ns	LEF
		530	15.70ms	LEP
(TT-2PyH$^+$NO$_3^-$)·H$_2$O	12	412	1.90 ns	HEF
		482	4.66 ms	MEP
		548	131.11 ms	LEP

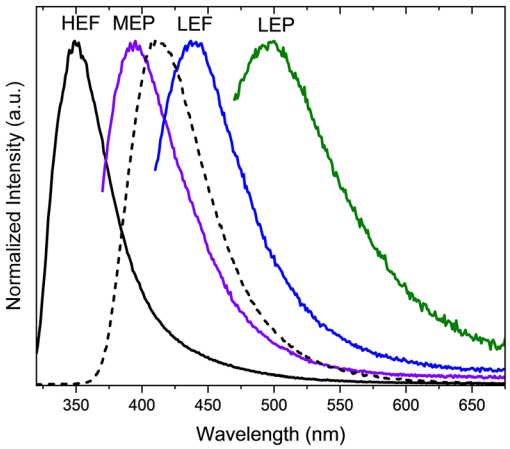

Fig. 1 Photophysical properties of **TT-2Py** in PMMA (**TT-2Py**/PMMA w/w 10%) before (solid lines) and after (dashed line) HCl exposure. Emission spectra λ_{exc} = 300 nm (black lines), λ_{exc} = 350 nm (violet), λ_{exc} = 390 nm (blue), and λ_{exc} = 450 nm (green).

phosphorescence) and LEF (low energy fluorescence), were associated with molecular electronic states.

Specifically, DFT calculations of **TT-2Py** revealed the presence of two almost isoenergetic minima (A and C, Fig. 2, left panel) on the S_0 potential energy surface (PES) of the molecule, separated by a very small energy barrier (B, ~2 kcal mol^{-1}). The more stable A conformation, with the pyridinic nitrogen atom pointing to the opposite site with respect to the **TT** one, corresponds to the X-ray structure observed in all the three polymorphs, while in C the two nitrogen atoms face each other. Consequently, HEF (clearly visible only in the PMMA film being overlapped with HEP in crystals) was associated (see Fig. 2, left panel) with radiative deactivation from the first singlet excited state (S_1) of molecules in the A conformation (representing the majority). HEP was explained as an anti-Kasha emission from a high energy triplet state (T_n) of ($\sigma/\pi,\pi^*$) character with slow internal conversion (IC) to the (π,π^*) T_1 one, from which MEP is originated. Finally, LEF was attributed to the fraction of molecules in the C minimum through excitation to a triplet T_m of low energy, followed by ISC to S_1. Though conformer C was not observed in any of the **TT-2Py** polymorphs, its minority presence cannot be excluded in blended films and, as a defect, in the crystal phase due to the low energy barrier from minimum A. This rather complex mechanism was also supported by pump–probe experiments.

Here, to further strengthen the hypothesis that conformational freedom is responsible for the appearance of dual fluorescence of **TT-2Py**, we have prepared and characterized its derivative with protonated pyridinic nitrogen, **TT-2PyH$^+$**, considering that H-bonds could lock the molecular geometry.

TT-2PyH$^+$NO$_3^-$ was synthesized by a reaction of **TT-2Py** with HNO_3 in DCM/MeOH (see the Experimental section) and characterized by single crystal X-ray diffraction and multinuclear ^{1}H, ^{13}C and ^{15}N NMR spectroscopy in DMSO-d$_6$ solution (see Fig. S12–S17). A comparison with the ^{1}H NMR of **TT-2Py** shows that after protonation all signals display a downfield shift ($\Delta\delta$ ~ 0.1–0.5 ppm) with the largest values for the H atoms

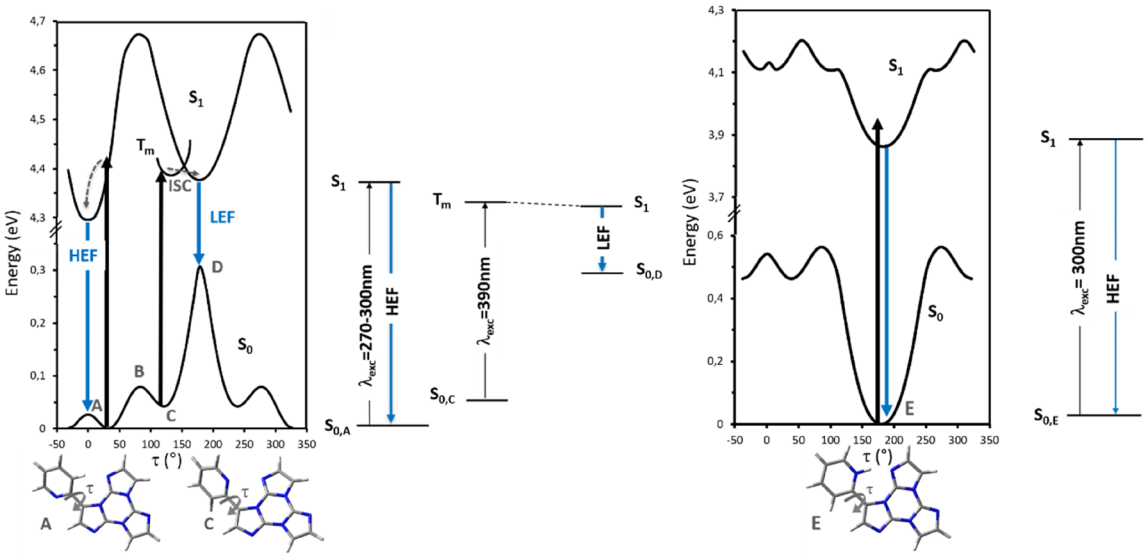

Fig. 2 Scans of the relaxed potential energy surfaces of S_1 and S_0 and simplified Jablonski diagrams for fluorescence emissions of **TT-2Py** (left) and **TT-2PyH$^+$** (right) along the N_{py}–C_{py}–C_{TT}–C_{TT} torsion angle, τ, at the (TD)-ωB97X/6-311++G(d,p) level of theory. T_m represents a generic triplet level, A, C and E denote minima on S_0 of **TT-2Py** and **TT-2PyH$^+$**, and B is the barrier between the two minima on S_0 of **TT-2Py**. Energies are relative to the S_0 state equilibrium geometry.

of the pyridine ring and for the singlet of the imidazole core (see Fig. 3). A similar effect was observed after complexation of **TT-2Py** to rhenium(I) carbonyl derivatives.[31] In addition, a triplet centered at 7.11 ppm, a characteristic NH^+ signal, with a J of 51.1 Hz due to ^{14}N–^1H coupling appears in the spectrum,[36] confirming that the structure is retained in DMSO-d_6 solution even though the integral value of the latter signal is slightly lower than the expected value, probably due to some exchange with deuterium.

^{15}N NMR spectroscopy performed by carrying out 2D ^1H–^{15}N heteronuclear long-range correlation (HMBC) experiments (Fig. S16 and S17) shows chemical shifts in the 150 and 220 ppm regions, respectively, assigned to the triazine-based core and the imidazole rings on the basis of previous studies,[37] together with a signal at 18 ppm due to the protonated pyridine nitrogen, while no signals in the 310 ppm region typical for the nitrogen resonance of pyridine have been detected.[38]

Single crystal X-ray diffraction studies performed at 150 and 299 K revealed that the compound crystallizes in the $P\bar{1}$ space group including, in its asymmetric unit, a water molecule (Fig. 4 and Table S1). In the **(TT-2PyH$^+$NO$_3^-$)·H$_2$O** crystal structure, the NO_3^- anion is hydrogen bonded (HB) to both imidazolic and pyridinic hydrogen atoms and the water molecule which, in turn, acts as a HB acceptor from a pyridinic hydrogen atom. The main difference between the 150 and 299 K structures is the presence of a minor disordered component of NO_3^- in the latter. **TT-2PyH$^+$** adopts a virtually planar and locked conformation thanks to the formation of a strong N–H$^+$···N intramolecular HB ($r_{H\cdots N}$ = 1.85 Å) bridging the protonated pyridinic nitrogen atom with the closest nitrogen of **TT**, generating a 7-membered cyclic structure. Thus, the hydrogen bond is the driving force to massively rotate, by almost 180°, the pyridinic moiety with respect to the orientation assumed in

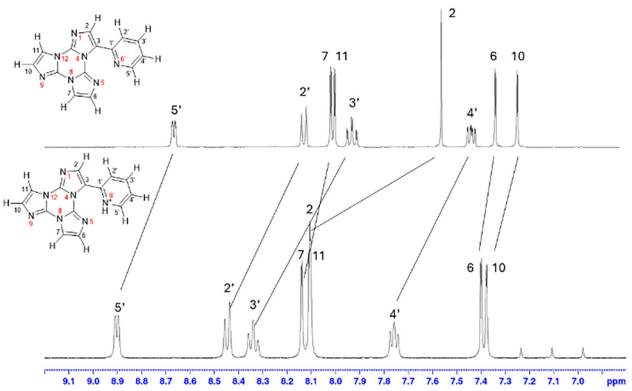

Fig. 3 ^{1}H-NMR spectra of **TT-2Py** (upper trace) and **TT-2PyH$^+$NO$_3^-$** (lower trace) (298 K, DMSO-d_6, 400 MHz).

TT-2Py (A minimum in Fig. 2, left panel). This locked structure was previously predicted by DFT scan calculations on the **TT-2PyH$^+$** S_0 PES (Fig. 2, right panel),[28] evidencing the great stabilization accompanying such rotation during the protonation process, leading to a single, deep well (E).

The chromophores are organized into infinite zig-zag ribbons through relatively strong centrosymmetric C–H···N HBs ($r_{H\cdots N}$ = 2.33 and 2.37 Å, see Fig. 4, top). Ribbons are laterally connected to each other through bridging NO_3^- counterions, lying almost in the same plane as that of the ribbons. As a result, infinite extended plates are formed, where the two ions, together with water which fills the spaces within ribbons, interdigitate forming a dense HB network ($r_{(C)H\cdots O(N)}$ in the 2.33–2.60 Å range, $r_{(C)H\cdots O(H)}$ = 2.45, 2.60 Å and $r_{(O)H\cdots O(N)^-}$ =1.92, 1.99 Å, parameters, here and below, referring to the structure determined at 150 K, see Table S2). The layers stack in a quite largely slipped head-to-tail arrangement of the **TT** units

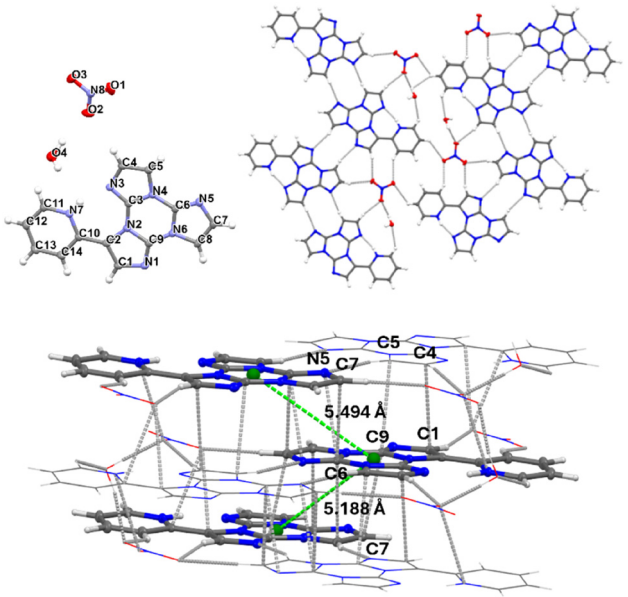

Fig. 4 Crystal structure of **(TT-2PyH$^+$NO$_3^-$)·H$_2$O** at 150 K: asymmetric unit (top left) and packing fragments showing the HB network (top right) and the π–π stacking motif highlighting the head-to-tail arrangement of the chromophores (bottom). Intermolecular contacts below the sum of vdW radii (dashed grey lines) and selected triazinic geometrical centroids (green spheres) are included. Ellipsoids at 20% probability.

(see Fig. 4, bottom), with alternating separations between the layers of 3.074 and 3.202 Å and the corresponding distances between triazinic geometrical centroids of 5.494 and 5.188 Å. Cations from adjacent layers overlap with the imidazolic subunits opposite to pyridine, with shortest contacts, $r_{C6\cdots C7(1-x,1-y,1-z)}$ = 3.200(2) Å, $r_{C6\cdots N5(1-x,1-y,1-z)}$ = 3.228(2) Å, from one side, and $r_{C9\cdots C7(1-x,2-y,1-z)}$ = 3.249(2) Å from the other side of the reference molecule. Additional short contacts with the H-bonded centrosymmetry-related equivalent ($r_{C1\cdots C4(1+x,y,z)}$ = 3.327(2) Å and $r_{C9\cdots C5(1+x,y,z)}$ = 3.389(2) Å) are found from both sides of the molecule. Such multiple short C···C and C···N distances along the crystallographic *b* axis denote the presence of columnar aggregates associated with the establishment of strong π–π stacking interactions among the chromophores, despite the large molecules' slippage. Quite similar stacking features have been found in polymorph A of the parent **TT-2Py** neutral derivative, displaying several C···C close contacts with a comparable distance (5.358 Å) between triazinic centroids. The anions are placed, along *b*, approximately halfway between two pyridinic rings, with the closest cation–anion centroids distance ($r_{C\cdots A}$) equal to 3.829 Å.

Intermolecular geometric parameters respond to temperature variation in quite a different way. Going from 150 to 299 K, $r_{C\cdots A}$ undergoes a large increase (0.1 Å) to 3.925 Å; the shortest C···C/N contacts display a usual 0.04–0.05 Å increase ($r_{C6\cdots C7(1-x,1-y,1-z)}$ = 3.252(3) Å, $r_{C9\cdots C7(1-x,2-y,1-z)}$ = 3.287(3) Å); and, notably, H-bonds linking the chromophores are virtually independent of temperature (see Table S2), indicating rigid interchromophoric connection through HB.[39–43]

To visualize and quantify the different intermolecular interactions governing the structure of **(TT-2PyH$^+$NO$_3^-$)·H$_2$O**, a

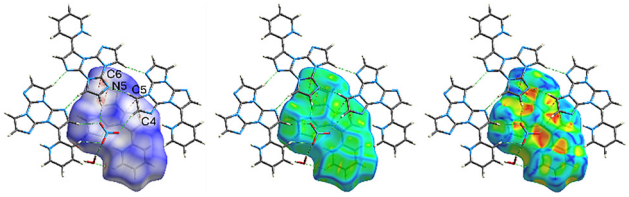

Fig. 5 Hirshfeld surface for **TT-2PyH$^+$** mapped with d_{norm} (left), curvedness (center) and shape index (right) with X···Y contacts and hydrogen bonds (red and green dashed lines, respectively) shorter than the sum of the vdW radii.

Hirshfeld surface (HS) analysis[44] has been performed. Particularly illuminating for the present structure are plots of HSs mapped with d_{norm}, curvedness (*C*) and shape index (*S*), where d_{norm} is the sum of normalised (with vdW radii) d_i and d_e, the distances from the Hirshfeld surface to the nearest nucleus inside and outside the surface, respectively. *C* and *S* are both defined in terms of the HS principal curvatures, the former depending on the root–mean–square curvature of the surface, and the latter providing a qualitative description of its shape, identifying complementary hollows (red) and bumps (blue regions), associated respectively with acceptor and donor entities of the interaction.[45] Fig. 5 shows HSs mapped with d_{norm}, *C* and *S* for **TT-2PyH$^+$** within the crystal, including for clarity the counterion, a water molecule and other protonated species interacting with the reference one along the stacking axis. The map with d_{norm} (Fig. 5, left) clearly indicates the strength and type of intermolecular interactions, with red regions (*i.e.* with distances shorter than the sum of vdW radii) being found in proximity of nitrogen and hydrogen atoms or over carbon atoms, and therefore attributable, respectively, to hydrogen bonds or π–π stacking interactions involving these atoms. The curvedness map (Fig. 5, center), characterized by extended green regions (*i.e.* having low curvature) separated by blue edges (large curvatures) gives evidence of the planar stacking between molecules. The patterns of red-orange spots on the shape index surface (Fig. 5, right) are diagnostic for close C···C/N interplanar contacts, denoting the areas involved in π–π stacking interaction.[46]

When excited at high energy (300-370 nm), crystals of **(TT-2PyH$^+$NO$_3^-$)·H$_2$O** display at room temperature a multicomponent broad emission (Fig. 6 and Table 1) comprising one fluorescence (at 412 nm, τ = 1.90 ns, Fig. S2) as a shoulder of a much stronger phosphorescence (at 482 nm, τ = 4.66 ms; overall Φ = 12%, Fig. S3), with the latter isolated by exciting at sufficiently low energy to exclude the high energy peak (λ_{exc} ~ 412 nm). By exciting at 480 nm an additional long-lived emission (at 548 nm, τ = 131.11 ms, Fig. S4), which is overwhelmed by the stronger high energy components at high energy excitations, appears in the spectrum. These spectral features, which are maintained at 77 K, can be considered as the red-shifted analogue of the neutral molecule HEF, MEP and LEP. The prolonging of lifetimes at low temperature (3.23 ns, 24.27 ms and 550 ms, respectively, Fig. S6–S8) indicates inhibition of thermal quenching especially for the long-lived components ($\tau_{77\,K}/\tau_{298\,K}$ = 1.7 for HEF, 5.2 for MEP and 4.2 for LEP).

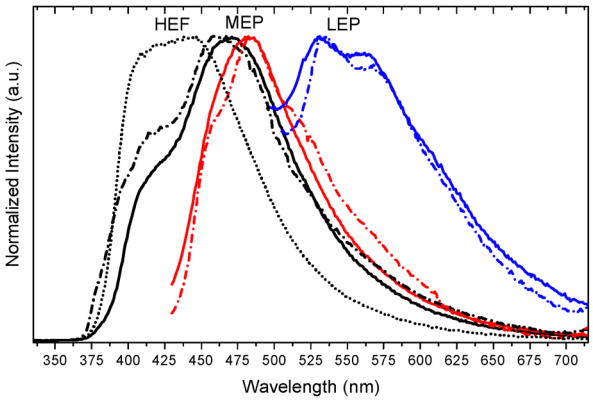

Fig. 6 The emission spectra of **(TT-2PyH$^+$NO$_3^-$)·H$_2$O** crystals at 298 K (full lines) and 77 K (dashed dotted lines); λ_{exc}: 300 nm (black lines), 412 nm (red lines) and 480 nm (blue lines). The emission spectrum of crystals after grinding at 298 K and 300 nm excitation is also reported (black dotted line).

The presence of only one minimum in both the **TT-2PyH$^+$** S_0 and S_1 PESs (Fig. 2, right panel) explains the observation of only one fluorescence (HEF) in crystals of **(TT-2PyH$^+$NO$_3^-$)·H$_2$O**. At the same time, the absence of LEF, resulting from locking the molecules in a rigid conformation through intramolecular HB, confirms molecular flexibility at its origin in **TT-2Py**. Moreover, in agreement with previously reported TDDFT calculations,[28] anti-Kasha HEP is not observed for **TT-2PyH$^+$** having only (π,π^*) levels (see Fig. S11 for a full picture of the **TT-2Py** and **TT-2PyH$^+$** electronic levels including Natural Transition Orbitals for selected transitions). The only observed molecular phosphorescence, MEP, is explained as radiative deactivation from T_1 reached, after IC, through easy ISC from S_1 to the almost overlapped T_4 level. These results also agree with what was previously observed for **TT-2Py**-blended PMMA films exposed to acidic vapors to give **TT-2PyH$^+$**, which showed a single fluorescence (at 412 nm, Fig. 1), together with a weak phosphorescence, both at lower energy with respect to the corresponding ones of **TT-2Py**.

Compared with the previous results on **TT-2PyH$^+$**/PMMA, the strong intensification of MEP relative to HEF in **TT-2PyH$^+$** crystals can be interpreted to be due to rigidification and protection from oxygen quenching through intermolecular interactions resulting in crystallization-induced features. Moreover, previous investigation on the effects of ion-pairing on the emissive properties of benzimidazolium salts demonstrated that a close cation–anion centroids distance, as observed in the present compound, favors molecular phosphorescence at the expense of the corresponding fluorescence.[47] A crystalline induced effect is supported by measurements on ground **TT-2PyH$^+$** crystals which display a slight increase in the overall quantum efficiency (14.5%) accompanied by a reduction of MEP intensity relative to HEF (Fig. S9) suggesting an easier singlet–triplet ISC process in crystalline **TT-2PyH$^+$**.

Materials and methods

All reagents and model molecules were purchased from chemical suppliers and used without further purification unless otherwise stated. **TT-2Py** was prepared according to literature procedures.[28]

The ^{1}H, ^{13}C and ^{15}N NMR spectra were recorded on a Bruker AVANCE-400 instrument (400 MHz). Chemical shifts are reported in parts per million (ppm) and are referenced to the residual solvent peak (DMSO, ^{1}H 2.50 ppm, ^{13}C 39.50 ppm) and to NH_3 for ^{15}N resonances. Coupling constants (J) are given in hertz (Hz) and are quoted to the nearest 0.5 Hz. Peak multiplicities are described in the following way: s, singlet; d, doublet; t. triplet; and m, multiplet.

Synthesis of TT-2PyH$^+$NO$_3^-$

TT-2Py (0.035 g, 0.127 mmol) was dissolved at room temperature in a 2 : 1 DCM(10 mL)/MeOH(5 mL) mixture inside a 25 mL round bottom flask equipped with a magnetic stirrer. Two drops of concentrated nitric acid were added to the mixture, which was kept under stirring for 1h at room temperature. Single crystals of **(TT-2PyH$^+$NO$_3^-$)·H$_2$O** suitable for XRD analysis were obtained in a few days by slow evaporation of the solvent mixture.

NMR data for **TT-2PyH$^+$NO$_3^-$** (9.4 T, DMSO-d$_6$, 298 K, δ, ppm): ^{1}H NMR 8.90 (d, J = 5.1, 1H), 8.44 (d, J = 8.1 Hz, 1H), 8.33 (m, 1H), 8.13 (d, J = 1.5 Hz, 1H), 8.10 (d, J = 1.5 Hz, 1H), 8.08 (s, 1H), 7.75 (m, 1H), 7.39 (d, J = 1.5 Hz, 1H), 7.37 (d, J = 1.5 Hz, 1H), 7.11 (t, J = 51.1 Hz, 1H). ^{13}C NMR: 144.89 (CH), 143.67 (C), 141.39 (CH), 138.28 (C), 136.00 (C), 135.47 (C), 133.05 (CH), 129.10 (CH), 127.18 (CH), 125.07 (CH), 124.18 (CH), 123.50 (C), 112.27 (CH), 112.09 (CH). ^{15}N NMR: 220.9, 219.0, 154.6, 150.2, 18.6 (Fig. S12–S17).

X-ray diffraction studies.

X-ray data of **(TT-2PyH$^+$NO$_3^-$)·H$_2$O** have been collected at 150 and 299 K on a Rigaku XtaLAB Synergy S X-ray diffractometer (Rigaku Co., Tokyo, Japan) operated with mirror-monochromated micro-focus Cu-Kα radiation (λ = 1.54184 Å) at 50 kV and 1.0 mA and equipped with a CCD HyPix 6000 detector. The structure has been solved using direct methods and refined with SHELXL-19[48] using a full-matrix least squares procedure based on F2 using all data. Hydrogen atoms have been placed at geometrically estimated positions. Details related to the crystal and the structural refinement are presented in Table S1. Full details of crystal data and structure refinement, in CIF format, are available in the SI. Hydrogen atoms were placed at geometrically estimated positions except those of the water co-crystallized molecule. Their position was refined by fixing the O–H and H···H distances with DFIX and DANG restraints, respectively. The crystal data and results of structural refinement are summarized in Table S1, while full details, in the CIF format, are available in the SI; CCDC reference numbers: 2401405 and 2401406 for the structures collected at 150 and 299 K, respectively.

Computational details

DFT and TDDFT calculations on isolated 'gas-phase' **TT-2PyH$^+$** ions were performed with the Gaussian 16 program (Revision A.03)[49] using the 6-311++G(d,p) basis set. Geometry

optimization has been carried out starting from the corresponding X-ray molecular structure. The ωB97X[50] functional was adopted throughout, owing to its good performance in describing not only ground and excited state properties (though slightly overestimating excitation electronic energies), but also intermolecular interactions including, in particular, π–π interactions. Further details are reported in the SI.

Photophysical characterization

Photoluminescence quantum yields have been measured using a C11347 Quantaurus–Absolute Photoluminescence Quantum Yield Spectrometer (Hamamatsu Photonics K.K), equipped with a 150 W Xenon lamp, an integrating sphere and a multichannel detector. Steady state emission and excitation spectra and photoluminescence lifetimes have been obtained using an FLS 980 (Edinburgh Instruments Ltd) spectrofluorimeter. The steady state measurements have been recorded using a 450 W Xenon arc lamp. Photoluminescence lifetime measurements have been performed using an EPLED-300 (Edinburgh Instruments Ltd) and a microsecond flash Xe-lamp (60 W, 0.1–100 Hz) with data acquisition devices based on time correlated single-photon counting (TCSPC) and multi-channel scaling (MCS) methods, respectively. Average lifetimes are obtained using $\tau_{av} = \frac{\sum A_i \tau_i^2}{\sum A_i \tau_i}$ from bi-exponential or three-exponential fits. Low temperature measurements have been performed by immersion of the sample in a liquid N_2 quartz dewar.

Conclusions

Intra- and intermolecular interactions play a key role in materials' photophysical behavior. Besides their proven ability to reduce competitive non-radiative deactivation channels, more subtle effects do exist and still need deeper investigation. In the present article, the effects of the HB and π–π stacking interactions on the emissive features of **TT-2Py** and **TT-2PyH$^+$** are disclosed. While π–π interactions activate ultralong phosphorescence in both compounds, the intramolecular HB in **TT-2PyH$^+$** is demonstrated to suppress, through conformational locking, the low energy fluorescence of **TT-2Py** as originally proposed. This work therefore provides a further contribution to understanding the relationship between molecular structures and photoluminescence performance at the molecular and aggregate levels.

Author contributions

Conceptualization: D. Mal., E. L., E. C. and A. F.; methodology: D. Mal., E. L., E. C. and A.F.; investigation: all authors; supervision: E. C. and A. F.; writing – original draft preparation: E. C. and A. F.; and writing – review and editing: all authors.

Conflicts of interest

There are no conflicts to declare.

Data availability

The data supporting this article have been included as part of the supplementary information (SI). Supplementary information: photophysical data, computational results, crystallographic data and NMR spectra. See DOI: https://doi.org/10.1039/d5cp03691g.

CCDC 2401405 and 2401406 contain the supplementary crystallographic data for this paper.[51a,b]

Acknowledgements

D. M. acknowledges Fondazione Cariplo for financial support (Giovani Ricercatori, 2024-0439). The use of instruments purchased through the Regione Lombardia – Fondazione Cariplo joint SmartMatLab Project is gratefully acknowledged. XRD data have been collected at the SCXRD facility of the Unitech COSPECT at the University of Milan (Italy).

Notes and references

1 Q. Dang, Y. Jiang, J. Wang, J. Wang, Q. Zhang, M. Zhang, S. Luo, Y. Xie, K. Pu, Q. Li and Z. Li, *Adv. Mater.*, 2020, **32**, 2006752.
2 W. Qin, P. Zhang, H. Li, J. W. Y. Lam, Y. Cai, R. T. K. Kwok, J. Qian, W. Zheng and B. Z. Tang, *Chem. Sci.*, 2018, **9**, 2705.
3 Y. Wang, H. Gao, J. Yang, M. Fang, D. Ding, B. Z. Tang and Z. Li, *Adv. Mater.*, 2021, **33**, 2007811.
4 L. Gu, H. Wu, H. Ma, W. Ye, W. Jia, H. Wang, H. Chen, N. Zhang, D. Wang, C. Qian, Z. An, W. Huang and Y. Zhao, *Nat. Commun.*, 2020, **11**, 944.
5 Y. Lei, W. Dai, J. Guan, S. Guo, F. Ren, Y. Zhou, J. Shi, B. Tong, Z. Cai, J. Zheng and Y. Dong, *Angew. Chem., Int. Ed.*, 2020, **59**, 16054.
6 Y. Li and P. Gao, *Chemosensors*, 2023, **11**, 489.
7 B. Sk and S. Hirata, *Adv. Sci.*, 2024, **11**, 2308897.
8 J. Tan, Q. Li, S. Meng, Y. Li, J. Yang, Y. Ye, Z. Tang, S. Qu and X. Ren, *Adv. Mater.*, 2021, **33**, 2006781.
9 S. Hirata, K. Totani, H. Kaji, M. Vacha, T. Watanabe and C. Adachi, *Adv. Opt. Mater.*, 2013, **1**, 438.
10 X. Ma, J. Wang and H. Tian, *Acc. Chem. Res.*, 2019, **52**, 738.
11 X.-K. Ma and Y. Liu, *Acc. Chem. Res.*, 2021, **54**, 3403.
12 H. Shi, W. Yao, W. Ye, H. Ma, W. Huang and Z. An, *Acc. Chem. Res.*, 2022, **55**, 3445.
13 X. Yang, G. I. N. Waterhouse, S. Lu and J. Yu, *Chem. Soc. Rev.*, 2023, **52**, 8005.
14 W. Zhao, Z. He and B. Z. Tang, *Nat. Rev. Mater.*, 2020, **5**, 869.
15 S. Cai, H. Shi, J. Li, L. Gu, Y. Ni, Z. Cheng, S. Wang, W.-W. Xiong, L. Li, Z. An and W. Huang, *Adv. Mater.*, 2017, **29**, 1701244.
16 S. Cai, X. Yao, H. Ma, H. Shi and Z. An, *Aggregate*, 2023, **4**, e320.
17 C. Demangeat, M. Remond, T. Roisnel, C. Quinton and L. Favereau, *Chem. – Eur. J.*, 2024, **30**, e202401506.

18 L. Gu, H. Shi, M. Gu, K. Ling, H. Ma, S. Cai, L. Song, C. Ma, H. Li, G. Xing, X. Hang, J. Li, Y. Gao, W. Yao, Z. Shuai, Z. An, X. Liu and W. Huang, *Angew. Chem., Int. Ed.*, 2018, **57**, 8425.
19 A. Jamadar, A. K. Singh, L. Roy and A. Das, *J. Mater. Chem. C*, 2021, **9**, 11893.
20 X.-N. Li, M. Yang, X.-L. Chen, J.-H. Jia, W.-W. Zhao, X.-Y. Wu, S.-S. Wang, L. Meng and C.-Z. Lu, *Small*, 2019, **15**, 1903270.
21 E. Lucenti, A. Forni, C. Botta, L. Carlucci, C. Giannini, D. Marinotto, A. Previtali, S. Righetto and E. Cariati, *J. Phys. Chem. Lett.*, 2017, **8**, 1894.
22 S. Sujilkumar, A. Kalyani and M. Hariharan, *Chem. Commun.*, 2025, **61**, 5463.
23 J. Zhou, L. Stojanović, A. A. Berezin, T. Battisti, A. Gill, B. M. Kariuki, D. Bonifazi, R. Crespo-Otero, M. R. Wasielewski and Y.-L. Wu, *Chem. Sci.*, 2021, **12**, 767.
24 Z. Chai, C. Wang, J. Wang, F. Liu, Y. Xie, Y.-Z. Zhang, J.-R. Li, Q. Li and Z. Li, *Chem. Sci.*, 2017, **8**, 8336.
25 M. Fang, J. Yang, X. Xiang, Y. Xie, Y. Dong, Q. Peng, Q. Li and Z. Li, *Mater. Chem. Front.*, 2018, **2**, 2124.
26 H. Li, J. Gu, Z. Wang, J. Wang, F. He, P. Li, Y. Tao, H. Li, G. Xie, W. Huang, C. Zheng and R. Chen, *Nat. Commun.*, 2022, **13**, 429.
27 A. Forni, D. Malpicci, D. Maver, E. Lucenti and E. Cariati, *J. Mater. Chem. C*, 2025, **13**, 3721.
28 E. Lucenti, A. Forni, A. Previtali, D. Marinotto, D. Malpicci, S. Righetto, C. Giannini, T. Virgili, P. Kabacinski, L. Ganzer, U. Giovanella, C. Botta and E. Cariati, *Chem. Sci.*, 2020, **11**, 7599.
29 D. Malpicci, S. R. Araneo, S. Arnaboldi, E. Cariati, A. Forni, S. Grecchi, E. Lucenti, D. Marinotto, D. Maver and P. R. Mussini, *Electrochim. Acta*, 2023, **469**, 143117.
30 D. Malpicci, D. Blasi, D. Marinotto, A. Forni, E. Cariati, E. Lucenti and L. Carlucci, *Crystals*, 2023, **13**, 149.
31 D. Malpicci, D. Maver, D. Maggioni, P. Mercandelli, L. Carlucci, E. Cariati, P. Mussini and M. Panigati, *New J. Chem.*, 2023, **47**, 21463.
32 E. Melnic, V. C. Kravtsov, E. Lucenti, E. Cariati, A. Forni, N. Siminel and M. S. Fonari, *New J. Chem.*, 2021, **45**, 9040.
33 M. S. Fonari, V. C. Kravtsov, V. Bold, E. Lucenti, E. Cariati, D. Marinotto and A. Forni, *Cryst. Growth Des.*, 2021, **21**, 4184.
34 E. Lucenti, E. Cariati, A. Previtali, D. Marinotto, A. Forni, V. Bold, V. C. Kravtsov, M. S. Fonari, S. Galli and L. Carlucci, *Cryst. Growth Des.*, 2019, **19**, 1567.
35 D. Malpicci, E. Lucenti, A. Forni, D. Marinotto, A. Previtali, L. Carlucci, P. Mercandelli, C. Botta, S. Righetto and E. Cariati, *Inorg. Chem. Front.*, 2021, **8**, 1312.
36 T. D. W. Claridge, in *High-Resolution NMR Techniques in Organic Chemistry*, ed. T. D. W. Claridge, Elsevier, Boston, 3rd edn, 2016, p. 243, DOI: 10.1016/B978-0-08-099986-9.00007-5.
37 S. Di Micco, C. Giannini, A. Previtali, E. Lucenti and G. Bifulco, *Magn. Reson. Chem.*, 2019, **57**, 82.
38 P. Beltrame, E. Cadoni, C. Floris, G. Gelli and A. Lai, *Spectrochim. Acta, Part A*, 2002, **58**, 2693.
39 S. Bhattacharya and B. K. Saha, *Cryst. Growth Des.*, 2013, **13**, 3299.
40 A. Forni, P. Metrangolo, T. Pilati and G. Resnati, *Cryst. Growth Des.*, 2004, **4**, 291.
41 V. G. Saraswatula and B. K. Saha, *New J. Chem.*, 2014, **38**, 897.
42 V. G. Saraswatula and B. K. Saha, *Chem. Commun.*, 2015, **51**, 9829.
43 V. G. Saraswatula, D. Sharada and B. K. Saha, *Cryst. Growth Des.*, 2018, **18**, 52.
44 P. R. Spackman, M. J. Turner, J. J. McKinnon, S. K. Wolff, D. J. Grimwood, D. Jayatilaka and M. A. Spackman, *J. Appl. Crystallogr.*, 2021, **54**, 1006.
45 M. A. Spackman and D. Jayatilaka, *CrystEngComm*, 2009, **11**, 19.
46 J. J. McKinnon, M. A. Spackman and A. S. Mitchell, *Acta Crystallogr., Sect. B: Struct. Sci.*, 2004, **60**, 627.
47 G. Di Carlo, A. Forni, P. Moretti, D. Marinotto, C. Botta, M. Pizzotti, F. Tessore and E. Cariati, *J. Mater. Chem. C*, 2021, **9**, 4182.
48 G. M. Sheldrick, *Acta Crystallogr., Sect. C: Struct. Chem.*, 2015, **71**, 3.
49 M. J. Frisch, G. W. Trucks, H. B. Schlegel, G. E. Scuseria, M. A. Robb, J. R. Cheeseman, G. Scalmani, V. Barone, G. A. Petersson, H. Nakatsuji, X. Li, M. Caricato, A. V. Marenich, J. Bloino, B. G. Janesko, R. Gomperts, B. Mennucci, H. P. Hratchian, J. V. Ortiz, A. F. Izmaylov, J. L. Sonnenberg, W. Williams, F. Ding, F. Lipparini, F. Egidi, J. Goings, B. Peng, A. Petrone, T. Henderson, D. Ranasinghe, V. G. Zakrzewski, J. Gao, N. Rega, G. Zheng, W. Liang, M. Hada, M. Ehara, K. Toyota, R. Fukuda, J. Hasegawa, M. Ishida, T. Nakajima, Y. Honda, O. Kitao, H. Nakai, T. Vreven, K. Throssell, J. A. Montgomery Jr., J. E. Peralta, F. Ogliaro, M. J. Bearpark, J. J. Heyd, E. N. Brothers, K. N. Kudin, V. N. Staroverov, T. A. Keith, R. Kobayashi, J. Normand, K. Raghavachari, A. P. Rendell, J. C. Burant, S. S. Iyengar, J. Tomasi, M. Cossi, J. M. Millam, M. Klene, C. Adamo, R. Cammi, J. W. Ochterski, R. L. Martin, K. Morokuma, O. Farkas, J. B. Foresman and D. J. Fox, *Gaussian 16 Rev. A.03*, Wallingford, CT, 2016.
50 J.-D. Chai and M. Head-Gordon, *J. Chem. Phys.*, 2008, **128**, 084106.
51 (*a*) CCDC 2401405: Experimental Crystal Structure Determination, 2025, DOI: 10.5517/ccdc.csd.cc2llvpr; (*b*) CCDC 2401406: Experimental Crystal Structure Determination, 2025, DOI: 10.5517/ccdc.csd.cc2llvqs.

